Reflection imaging of the Moon's interior using deep-moonquake seismic interferometry

Nishitsuji, Yohei; Rowe, CA; Wapenaar, Kees; Draganov, Deyan

DOI
10.1002/2015JE004975

Publication date
2016

Document Version
Final published version

Published in
Journal of Geophysical Research Planets

AGU PUBLICATIONS

JGR

Journal of Geophysical Research: Planets

RESEARCH ARTICLE
10.1002/2015JE004975

Key Points:
- We apply the first body-wave seismic interferometry to deep moonquakes
- Moho reflection is imaged around 50 km depth beneath the Apollo stations
- Possible scattering zone is imaged where the shallow moonquakes occur

Correspondence to:
Y. Nishitsuji,
y.nishitsuji@tudelft.nl

Citation:
Nishitsuji, Y., C. A. Rowe, K. Wapenaar, and D. Draganov (2016), Reflection imaging of the Moon's interior using deep-moonquake seismic interferometry, *J. Geophys. Res. Planets*, *121*, 695–713, doi:10.1002/2015JE004975.

Received 4 NOV 2015
Accepted 6 APR 2016
Accepted article online 9 APR 2016
Published online 28 APR 2016

Reflection imaging of the Moon's interior using deep-moonquake seismic interferometry

Yohei Nishitsuji[1], C. A. Rowe[2], Kees Wapenaar[1], and Deyan Draganov[1]

[1]Department of Geoscience and Engineering, Delft University of Technology, Delft, Netherlands, [2]Earth and Environmental Sciences Division, Los Alamos National Laboratory, Los Alamos, New Mexico, USA

Abstract The internal structure of the Moon has been investigated over many years using a variety of seismic methods, such as travel time analysis, receiver functions, and tomography. Here we propose to apply body-wave seismic interferometry to deep moonquakes in order to retrieve zero-offset reflection responses (and thus images) beneath the Apollo stations on the nearside of the Moon from virtual sources colocated with the stations. This method is called deep-moonquake seismic interferometry (DMSI). Our results show a laterally coherent acoustic boundary around 50 km depth beneath all four Apollo stations. We interpret this boundary as the lunar seismic Moho. This depth agrees with Japan Aerospace Exploration Agency's (JAXA) SELenological and Engineering Explorer (SELENE) result and previous travel time analysis at the Apollo 12/14 sites. The deeper part of the image we obtain from DMSI shows laterally incoherent structures. Such lateral inhomogeneity we interpret as representing a zone characterized by strong scattering and constant apparent seismic velocity at our resolution scale (0.2–2.0 Hz).

1. Introduction

During the NASA Apollo missions, seismometers were installed on the Moon which transmitted continuous seismic data to the Earth between July 1969 and September 1977. Early analyses of the data resulted in identification of four types of natural moonquakes: meteoroid impacts [e.g., *Goins*, 1978; *Horvath et al.*, 1980; *Nakamura et al.*, 1981, 1982], thermal moonquakes [e.g., *Nakamura et al.*, 1982], shallow moonquakes [e.g., *Goins*, 1978; *Horvath et al.*, 1980; *Nakamura et al.*, 1982], and deep moonquakes [e.g., *Chapman et al.*, 1974; *Nakamura et al.*, 1981, 1982; *Bulow et al.*, 2005, 2007].

While only 28 shallow moonquakes (hypocenters at depths between 2 km and 220 km; [*Nakamura et al.*, 1981]) were detected from the records, 7083 deep moonquakes (hypocenters at depths between 700 km and 1200 km; [*Khan et al.*, 2013]) have been identified so far. It was also observed that the deep moonquakes appear to occur in spatially limited clusters, rather than being ubiquitously distributed [e.g., *Chapman et al.*, 1974; *Nakamura et al.*, 1981].

The data from the deep moonquakes have been examined using a variety of seismic methods for the purpose of determining the lunar structure, including travel time analysis [e.g., *Toksöz et al.*, 1974; *Goins et al.*, 1981; *Nakamura*, 1983; *Weber et al.*, 2011], receiver functions [*Vinnik*, 2001], and 3-D tomography [e.g., *Zhao et al.*, 2008]. Seismic interferometry (SI) using ambient noise has also been employed using these data [*Larose et al.*, 2005; *Tanimoto et al.*, 2008; *Sens-Schönfelder and Larose*, 2010; *Obermann et al.*, 2013]. In these analyses, the authors successfully retrieved higher-frequency Rayleigh waves (Rg) and characterized near-surface shear velocity through the resulting dispersion curves. Heretofore, SI methods have not been employed for retrieval of body-wave information to illuminate lunar structure.

In this study we analyze deep-moonquake seismograms. We apply body-wave SI [e.g., *Claerbout*, 1968; *Wapenaar et al.*, 2008; *Schuster*, 2009] via autocorrelation of the first *P* wave phase to the *P* wave coda. This allows us to retrieve the zero-offset subsurface reflection response from virtual sources colocated with the Apollo stations. For the sake of shorthand notation, we term this technique deep-moonquake seismic interferometry (DMSI). Obtaining virtual reflection responses of the Moon beneath the Apollo stations obviates the need for active seismic sources, such as explosives and artificial impacts recorded by the Apollo instruments.

Our goal is to identify the lunar seismic Moho using the DMSI technique. Knowledge of the crustal thickness is important to the understanding of the evolution of the Moon; it has implications for bulk composition, petrogenesis, and other aspects of lunar evolution. Previous studies using various seismic methods have reported widely

varying values of crustal thickness (depth of the Moho). *Toksöz et al*. [1972] reported an estimated depth to lunar Moho of 65 km based on *P* wave travel times from artificial impact sources (S-IVB booster and Lunar Module (LM) ascent stage); they later revised this in *Toksöz et al*. [1974], with a mean crustal thickness estimate of 60 km, based on travel time analysis and comparison to synthetic seismograms. *Nakamura* [1983] found a crustal thickness of 58 km at the Apollo 12/14 sites, whereas *Chenet et al*. [2006] and *Longnonné et al*. [2003] reported a thinner crust of 30–33 km. On the other hand, *Khan et al*. [2000] as well as Japan Aerospace Exploration Agency's (JAXA) SELenological and ENgineering Explorer (SELENE) reported by *Ishihara et al*. [2009] suggest values of 45–50 km. In addition, a recent gravity and topography study, Gravity Recovery And Interior Laboratory (GRAIL) operated by NASA, estimated the lunar crustal thickness to be 30–38 km [*Wieczorek et al*., 2013].

We are also interested in imaging the upper mantle, where the seismic velocity model is not well constrained [e.g., *Toksöz*, 1974; *Goins et al*., 1981] or is estimated to be roughly constant [e.g., *Weber et al*., 2011]. The reflection imaging using DMSI at these depths might provide some insight not only regarding the internal structure but also the mechanism of the shallow moonquakes, whose hypocentral depth estimates put them in the upper mantle. Researchers seem to have reached a consensus that tidal stress is a primary contributor to the genesis of deep moonquakes [e.g., *Toksöz et al*., 1977; *Frohlich and Nakamura*, 2009; *Weber et al*., 2009]; however, the source mechanism is still unclear for shallow moonquakes. It is clear that the crust and upper mantle exhibit a very high quality factor, *Q*, (low attenuation) compared to Earth [e.g., *Dainty et al*., 1974; *Nakamura et al*., 1976; *Goins et al*., 1981]. This suggests that a considerable degree of seismic scattering can be anticipated for the source region of the shallow moonquakes. Note that the scattering properties between the shallow crust [e.g., depth of 25 km in *Dainty et al*., 1974] and below the crust would be substantially different. While scattering in the shallow crust is expected to come from the fracturing of the crust by years of impacts, scattering originating below the crust would likely come from compositional heterogeneities, rather than mechanical fractures [*Besserer et al*., 2014].

Our DMSI study may be the first reflection imaging of the shallow Moon using natural sources like moonquakes. By reflections, we mean the energy generated by a source (either active or virtual) at the surface, which propagates into the subsurface, is reflected by an impedance contrast at a certain depth and is recorded at the surface. In the nomenclature of *Weber et al*. [2011], we use reflections *PxP* where *x* can be any impedance contrast. In the following, we describe how we apply the method to the deep moonquakes and obtain zero-offset reflection imaging beneath the Apollo stations.

2. Study Area and Data

Figure 1 presents a map of the nearside of the Moon where the Passive Seismic Experiment of the Apollo missions (12 and 14–16 in the cyan triangles) was carried out. In this study, we analyze seven clusters of the deep moonquakes whose wavefronts can be approximated as nearly planar when they arrive at the stations (ray parameters are smaller than 0.36 s deg^{-1}). Note that the angle degree we use in this study is for the Moon, whose radius is 1737 km (hence, 1° corresponds to approximately 30 km on the surface). Cluster centroids, including their location uncertainties, are also shown in Figure 1 [after *Nakamura*, 2005]. The uncertainty bars indicate the range of location scatter within each of the clusters. Numbers in the yellow rectangles indicate the depth with the uncertainties of the centroid of each cluster. In Figure 2, we show two extremes, among the clusters we analyzed, for one-way travel time curves using a recent 1-D velocity model published by *Weber et al*. [2011]. The curves are for the largest (0.36 s deg^{-1}) and smallest (0.04 s deg^{-1}) ray parameters, characterizing responses from cluster A15 recorded at Apollo station 14 (shown in blue) and responses from cluster A97 recorded at Apollo station 16 (shown in red). The one-way travel times for the *P* and *S* phases are extracted from these curves at the respective epicentral distances for A15 and A97 of 14.3° and 2.5°.

Seismic data of the deep moonquakes were collected using the Moon Seismic Monitor (http://darts.isas.jaxa.jp/planet/seismology/apollo/app/) of the Data Archives and Transmission System (DATS, darts.jaxa.jp), provided by the Center for Science-satellite Operation and Data Archive (C-SODA, http://c-soda.isas.jaxa.jp) at the Institute of Space and Astronautical Science (ISAS, http://www.isas.jaxa.jp/e/index.shtml) and the Japan Aerospace Exploration Agency (JAXA, http://global.jaxa.jp). We refer to the event catalog of the deep moonquakes, which is summarized by *Nakamura et al*. [1981] and also contains additional events identified by *Bulow et al*. [2005, 2007], to extract the event hypocenters of the aforementioned clusters. Since it is known that each cluster generally exhibits repeatable waveforms (deep moonquakes),

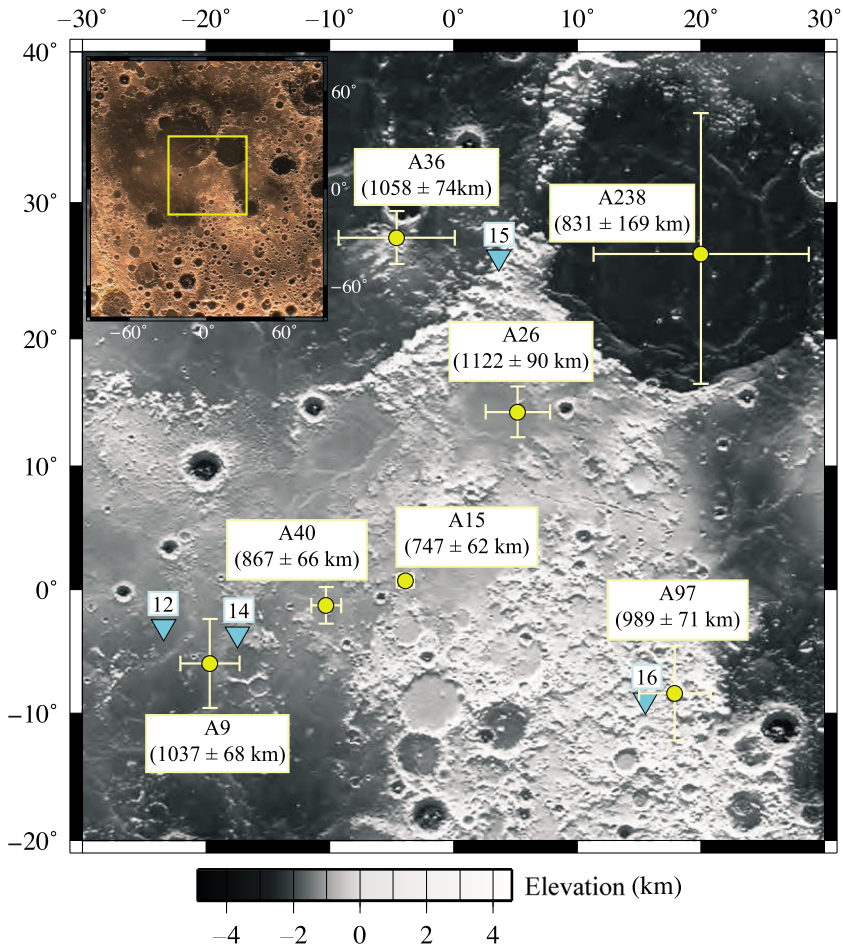

Figure 1. Spatial distribution of the seven clusters (labeled with capital A and a number) of deep moonquakes (yellow circles) used in our study. The numbers in the parentheses indicate depths of the clusters. Yellow bars indicate a lateral distribution range of deep moonquakes within the clusters calculated using *Nakamura* [2005]. Cyan triangles identify the locations of the Apollo seismic stations. Topography data, referenced to a Moon sphere (radius is 1737 km) whose origin is set to the center of mass, were taken from *Araki et al.* [2009].

the event identification was carried out via cross correlation using a single-event approach [*Bulow et al.*, 2005, 2007; *Nakamura et al.*, 1981].

In Table 1, we show a summary of the cluster coordinates and the Apollo stations for which each cluster is used. The epicentral distances and the ray parameters were calculated using mean values of the event locations. Note that cluster A40 is not used with station 14, because the number of events selected for DMSI after our quality control (QC) was too low. The complete list of the used deep moonquakes is given in Table 2.

3. Deep-Moonquake Seismic Interferometry

SI is more commonly defined as a method to retrieve new seismic records by correlation with existing records. In the context of seismic exploration, *Claerbout* [1968] showed that the zero-offset (source and receiver locations are colocated) reflection response of a horizontally layered (1-D) medium could be obtained from the autocorrelation of the transmission response measured at that location from noise sources in the subsurface. He termed this technique acoustic daylight imaging. As *Yokoi and Margaryan* [2008] demonstrated, acoustic daylight imaging applied for retrieval of surface waves is related to the spatial autocorrelation method. The latter was first introduced by *Aki* [1957], who estimated the subsoil structure from ambient vibration (microtremor) records. *Wapenaar* [2003, 2004] generalized Claerbout's acoustic daylight principle to any 3-D inhomogeneous medium and showed that, in the general case, cross correlation should be used from recordings of transient or noise sources that effectively

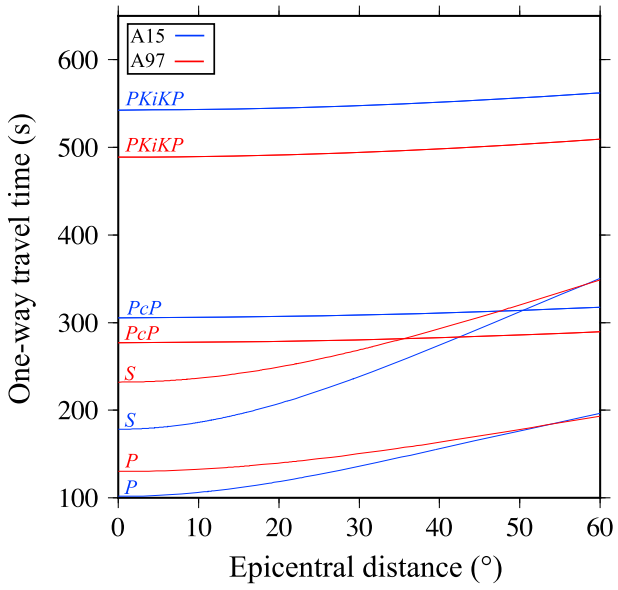

Figure 2. Expected one-way travel time of several phases from deep moonquakes as a function of epicentral distance. Blue curves are for cluster A15, whose direct *P* wave phase is expected to have the largest ray parameter (0.36 s deg^{-1}) at the closest receiver (Station 14). A15 is at 14.3° epicentral distance from Station 14. Red curves are for cluster A97, whose direct *P* wave phase will have the smallest ray parameter (0.04 s deg^{-1}) at the nearest receiver (Station 16). A97 is at 2.5° epicentral distance from Station 16. The velocity model for both *P* and *S* phases is taken from *Weber et al.* [2011].

surround the receivers. This method was then termed SI [*Schuster et al.*, 2004]. Recent work has shown that to remedy some limitations of the correlation method, such as irregular source illumination and intrinsic losses in the medium, SI by multidimensional deconvolution could be used [*Wapenaar et al.*, 2008].

DMSI, which we use here, is a specific application of SI by correlation for a 3-D medium. Still, it resembles closely the original acoustic daylight imaging. While the acoustic daylight imaging uses ambient noise in a 1-D situation, DMSI uses the *P* wave coda of the deep moonquakes in the 3-D approach. DMSI is also closely related to the global-phase seismic interferometry (GloPSI) method, as introduced by *Ruigrok and Wapenaar* [2012], to image the Moho under the Himalayas and Tibet. While GloPSI uses global phases, however, such as *PKP*, *PKiKP*, and *PKIKP*, DMSI uses the *P* wave coda.

To retrieve the zero-offset reflection response from DMSI with the full transmission response, in the general SI-by-correlation relation we use autocorrelation. For an acoustic 3-D medium and transient sources in the subsurface (like moonquakes), the discretized version of the relation in *Wapenaar* [2003] can be written as

$$\sum_k \{T(\mathbf{x}_R, \mathbf{x}_k, -t) * T(\mathbf{x}_R, \mathbf{x}_k, t)\} = \delta(t) - R(\mathbf{x}_R, \mathbf{x}_R, -t) - R(\mathbf{x}_R, \mathbf{x}_R, t), \quad (1)$$

where $T(\mathbf{x}_R, \mathbf{x}_k, t)$ is the transmission response at the receiver location $\mathbf{x}_R$ from a moonquake at location $\mathbf{x}_k$, k denotes the kth moonquake, $R(\mathbf{x}_R, \mathbf{x}_R, t)$ is the zero-offset reflection response for colocated source and receiver at location $\mathbf{x}_R$, $\delta(t)$ is the delta function, and * denotes convolution.

Equation (1) assumes that the receivers are at the Moon's (free) surface, while the sources are distributed along a boundary in the subsurface and are in the far field of the receivers. But this is quite an idealized situation, as moonquakes and earthquakes often occur along specific structures only. *Snieder* [2004] showed that the retrieved reflection energy in the result from SI comes from sources lying inside the stationary-phase zones. For a subsurface, whose structure is composed of horizontal or gently dipping reflectors, the stationary-phase zone for a zero-offset reflection at location $\mathbf{x}_R$ is around or close to the vertical below $\mathbf{x}_R$. This is because a station colocated with an active source would record only reflection energy that is characterized by vertical or near-vertical incidence.

Table 1. Seven Deep-Moonquake Clusters Used in This Study

Cluster ID	Latitude (°N)	Longitude (°E)	Depth (km)	Before QC No. of Events	After QC No. of Events	Discarded Events %	Apollo Station	Epicentral Distance (deg)	Ray Parameter (s deg^{-1})
A9	−6.0 ± 2.4	−19.7 ± 3.6	1037 ± 68	129	23	82	14	3.2	0.04
A15	0.7 ± 0.7	−3.9 ± 0.6	747 ± 62	50	7	86	14	14.3	0.36
A26	14.3 ± 2.6	5.2 ± 2.0	1122 ± 90	54	27	50	15	11.9	0.12
A36	27.5 ± 4.7	−4.6 ± 1.9	1058 ± 74	43	26	40	15	7.5	0.09
A40	−1.3 ± 1.2	−10.3 ± 1.5	867 ± 66	35	27	23	12	13.3	0.15
A97	−8.4 ± 2.9	17.9 ± 3.8	989 ± 71	45	14	69	16	2.5	0.04
A238	26.3 ± 8.7	20.0 ± 9.8	831 ± 169	36	20	44	15	14.7	0.30

Table 2. The 144 Deep-Moonquake Clusters Used in This Study

Cluster ID	Year	Month	Day	Hour	Minute	Apollo Station
A9	1971	04	04	13	22	14
A9	1971	04	30	08	40	14
A9	1971	05	27	13	27	14
A9	1971	05	28	20	02	14
A9	1971	06	23	15	07	14
A9	1971	07	20	21	23	14
A9	1971	07	22	09	19	14
A9	1971	08	18	22	31	14
A9	1971	09	15	08	52	14
A9	1971	11	07	16	04	14
A9	1971	12	04	22	32	14
A9	1972	04	19	04	27	14
A9	1972	09	28	17	39	14
A9	1974	06	16	09	38	14
A9	1974	10	03	09	04	14
A9	1974	10	30	11	23	14
A9	1974	12	24	12	00	14
A9	1975	11	15	12	16	14
A9	1976	03	03	03	38	14
A9	1977	01	23	04	38	14
A9	1977	01	24	15	52	14
A9	1977	02	20	20	12	14
A9	1977	04	16	20	02	14
A15	1971	03	24	02	58	14
A15	1972	10	22	18	45	14
A15	1973	05	05	08	59	14
A15	1974	09	12	01	29	14
A15	1974	11	30	18	12	14
A15	1974	12	29	04	43	14
A15	1976	07	05	18	26	14
A26	1971	09	26	02	09	15
A26	1971	09	26	22	02	15
A26	1971	10	24	17	10	15
A26	1971	11	02	16	53	15
A26	1971	11	09	12	41	15
A26	1971	11	16	17	22	15
A26	1971	11	21	01	46	15
A26	1971	11	21	17	57	15
A26	1972	01	11	08	52	15
A26	1972	03	19	04	45	15
A26	1972	04	04	05	05	15
A26	1972	04	29	18	10	15
A26	1972	08	05	12	57	15
A26	1973	02	16	02	27	15
A26	1973	11	09	16	40	15
A26	1974	02	27	16	09	15
A26	1974	10	14	01	36	15
A26	1974	10	23	00	58	15
A26	1975	05	09	02	37	15
A26	1975	05	12	17	02	15
A26	1975	05	24	14	00	15
A26	1975	10	06	06	05	15
A26	1977	03	31	12	17	15
A26	1977	04	01	22	42	15
A26	1977	06	20	14	54	15
A26	1977	07	19	23	07	15
A26	1977	09	09	10	37	15
A36	1971	08	04	03	27	15
A36	1971	09	28	20	32	15
A36	1971	09	30	02	11	15
A36	1971	09	30	18	19	15

Table 2. (continued)

Cluster ID	Year	Month	Day	Hour	Minute	Apollo Station
A36	1971	11	22	07	53	15
A36	1971	11	24	22	57	15
A36	1971	12	21	18	58	15
A36	1972	01	14	17	09	15
A36	1972	01	17	06	21	15
A36	1972	03	10	05	37	15
A36	1972	03	12	12	49	15
A36	1972	04	06	19	47	15
A36	1972	04	09	11	01	15
A36	1972	05	04	10	40	15
A36	1972	05	07	15	13	15
A36	1972	05	08	16	24	15
A36	1972	05	31	11	28	15
A36	1972	12	29	12	57	15
A36	1973	03	30	12	53	15
A36	1977	03	05	03	13	15
A36	1977	05	01	07	42	15
A36	1977	06	24	01	15	15
A36	1977	07	20	22	50	15
A36	1977	07	20	23	43	15
A36	1977	07	23	07	35	15
A36	1977	09	14	16	23	15
A40	1970	08	13	21	38	12
A40	1972	04	15	16	15	12
A40	1972	06	07	14	13	12
A40	1972	07	05	17	45	12
A40	1972	07	08	06	37	12
A40	1972	08	02	14	16	12
A40	1972	08	29	08	46	12
A40	1972	10	23	21	44	12
A40	1973	01	14	22	29	12
A40	1973	02	11	16	47	12
A40	1973	03	09	18	38	12
A40	1973	04	04	24	00	12
A40	1973	05	02	10	27	12
A40	1973	05	30	10	20	12
A40	1973	06	24	11	45	12
A40	1973	06	27	23	51	12
A40	1973	07	12	06	28	12
A40	1973	07	26	06	45	12
A40	1973	08	22	18	50	12
A40	1973	09	18	10	42	12
A40	1973	12	08	23	08	12
A40	1974	04	25	00	36	12
A40	1974	05	22	08	07	12
A40	1976	06	05	15	35	12
A40	1976	07	01	14	13	12
A40	1976	07	27	21	12	12
A40	1976	09	21	10	26	12
A97	1974	12	11	19	18	16
A97	1975	04	27	00	28	16
A97	1975	05	07	01	05	16
A97	1975	05	24	12	07	16
A97	1975	06	07	17	22	16
A97	1975	06	20	09	27	16
A97	1975	07	04	22	42	16
A97	1975	08	01	07	15	16
A97	1976	03	07	04	43	16
A97	1976	05	01	01	13	16
A97	1977	03	25	04	37	16
A97	1977	04	05	20	32	16

Table 2. (continued)

Cluster ID	Year	Month	Day	Hour	Minute	Apollo Station
A97	1977	05	19	06	11	16
A97	1977	06	11	12	33	16
A238	1971	08	05	01	28	15
A238	1971	09	01	13	40	15
A238	1971	11	23	14	37	15
A238	1972	03	11	03	15	15
A238	1972	04	08	01	55	15
A238	1972	06	28	13	03	15
A238	1972	07	25	16	26	15
A238	1973	01	04	10	55	15
A238	1973	01	31	16	27	15
A238	1973	02	02	21	00	15
A238	1973	03	02	10	30	15
A238	1973	03	30	00	46	15
A238	1973	03	30	01	06	15
A238	1973	04	26	14	48	15
A238	1973	10	02	16	08	15
A238	1976	09	23	09	59	15
A238	1977	03	06	17	25	15
A238	1977	04	02	19	38	15
A238	1977	07	22	08	05	15
A238	1977	08	18	05	50	15

In a 3-D medium, the stationary-phase zone is a patch. But even such a patch is, in general, unlikely to be sampled well with moonquakes, as the moonquakes cluster around certain locations (see Figure 1). Because of this clustering, applying equation (1) directly to clusters that may not be sufficiently close to an Apollo station (e.g., cluster A15 for station 14 and A238 for station 15) might result in an erroneously retrieved zero-offset reflection response because the cluster(s) may be outside the stationary-phase zone. Thus, the strongest contributions to the result, arising from the summation of the autocorrelations of a direct *P* wave phase and its free-surface reverberation between the Moon's surface and a subsurface reflector (primary reverberation), would not interfere constructively (stack) optimally. The result would be a reflection at a slightly erroneous time. Due to the source-receiver configuration of this study, we consider the stationary-phase zone for retrieving a zero-offset reflection. The extent of the stationary-phase zone depends on the depth of the reflectors and the depth of the moonquakes [e.g., *Kimman and Trampert*, 2010]. Taking an average velocity of 7.7 km/s and center frequency of 0.5 Hz, and a source depth of 800 km, we calculate that the stationary-phase zone for a reflector at a depth of 40 km (e.g., the Moho depth in *Weber et al.* [2011]) will have a radius of 212 km.

This effect can be minimized by targeting the zero-offset plane-wave response as in GloPSI [*Ruigrok and Wapenaar*, 2012]. The authors achieved this by choosing global phases, as these phases will have a planar wavefront at the recording stations and will be arriving nearly vertically. Summation over a sufficient number of ray parameters and azimuths ensures retrieval of the zero-offset (near) vertical-incidence plane-wave response.

Using deep moonquakes close to the Apollo stations ensures that the recorded transmission responses of *P* wave phases are nearly vertical (see Figure 2). Due to the clustering of the deep moonquakes, however, it is not possible to average over a sufficient number of ray parameters and azimuths. To remedy this, we select the *P* wave coda from direct *P* wave phases whose ray parameters are smaller than 0.36 (s deg^{-1}). The coda from such direct phases would be characterized by even smaller ray parameters and thus we can assume that the *P* wave coda reverberates nearly vertically between the reflectors in the subsurface and a station at the surface. To describe the use of only coda from the direct *P* wave phase, we rewrite equation (1) as

$$\sum_k \{T^c(\mathbf{x}_R, \mathbf{x}_k, -t) * T^c(\mathbf{x}_R, \mathbf{x}_k, t) * M_k(-t) * M_k(t)\} \propto, \\ \{\delta(t) - R(\mathbf{x}_R, \mathbf{x}_R, -t) - R(\mathbf{x}_R, \mathbf{x}_R, t)\} * \overline{M}_k(t) \tag{2}$$

where $T^c(\mathbf{x}_R, \mathbf{x}_k, t)$ is the selected *P* wave coda at receiver location $\mathbf{x}_R$ from a deep moonquake at $\mathbf{x}_k$ from one cluster, $M_k(t)$ is the source time function of the *k*th deep moonquake, and $\overline{M}_k(t)$ is the average of the autocorrelations for the different source time functions of the deep moonquakes in the cluster. A cartoon in

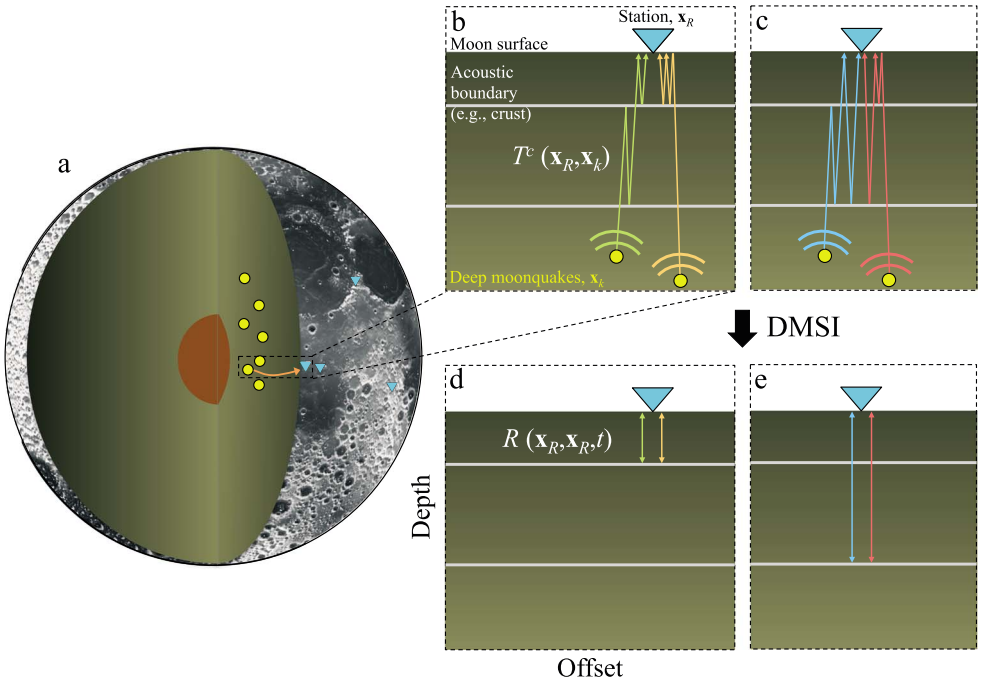

Figure 3. Cartoon illustrating how deep-moonquake seismic interferometry (DMSI) works. (a) Deep-moonquake clusters closest to an Apollo station are selected (ray parameter of the direct *P* wave phase is smaller than 0.36 s deg^{-1}). Topography data are taken from *Araki et al.* [2009]. (b) Schematic raypaths of two types of *P* wave coda arrivals: a reverberation between two reflectors and its free-surface reverberation from a shallow reflector (green); a first-order and a second-order free-surface reverberation from the shallow reflector (orange). (c) Schematic raypaths of two other types of *P* wave coda arrivals: the reverberation between two reflectors and its free-surface reverberation from a deep reflector (blue); a first-order free-surface reverberation from the shallow reflector and its free-surface reverberation from the deep reflector (red). (d) Retrieved zero-offset plane-wave reflection response beneath the station from the autocorrelation of the green and orange coda arrivals illustrated in Figure 3b. Summation over all such coda arrivals would retrieve the zero-offset vertical plane-wave response obtained from DMSI. (e) Same as in Figure 3d but using the coda arrivals in Figure 3c. Note that the horizontal and vertical axes in Figures 3b–3d are not in scale to the actual coordinate.

Figure 3 shows schematically how DMSI with coda, but without the direct *P* wave phase, functions. Note that the exclusion of the direct arrival, in our case the *P* phase, from the DMSI equation (1), might result in stronger nonphysical arrivals (artifacts) appearing in the retrieved result using DMSI as in equation (2). Such artifacts may be retrieved from the correlation of two primary reverberations (the first free-surface multiples of the direct *P* wave phase after bouncing at some impedance contrasts), for example. If the cluster is not situated in the stationary-phase zone, such artifacts will be weakened during the summation over the used cluster moonquakes because of the varying hypocentral depths and locations. The retrieved physical energy will result from correlation of multiply scattered arrivals, which, because of the multiple scattering, is characterized by smaller ray parameters and thus will sum constructively for more (or all) moonquakes in the cluster. Even if the artifacts are strong compared to the retrieved physical energy, the artifacts are normally strongest at the earlier times (close to time 0 s) [e.g., *Draganov et al.*, 2010], while the later times are less affected. In the following sections, we apply DMSI following equation (2).

4. Data Processing

We begin by deconvolving the instrument response. For this we use the instrument information given by *Latham et al.* [1969], as well as by Incorporated Research Institutions for Seismology (IRIS) Data Management Center, and we obtain the three-component (two orthogonal horizontal and one vertical) data set. Following *Nakamura* [2005], we apply a fifth-order Butterworth band-pass filter between 0.2 and 2 Hz to improve the signal-to-noise ratio (SNR) of the deep-moonquake phases. The 2 Hz upper limit is dictated by expected strong scattering due to the megaregolith [*Blanchette-Guertin et al.*, 2012]. Figure 4a shows an example of a raw seismogram as recorded by the vertical component of the Apollo 12 station for a deep

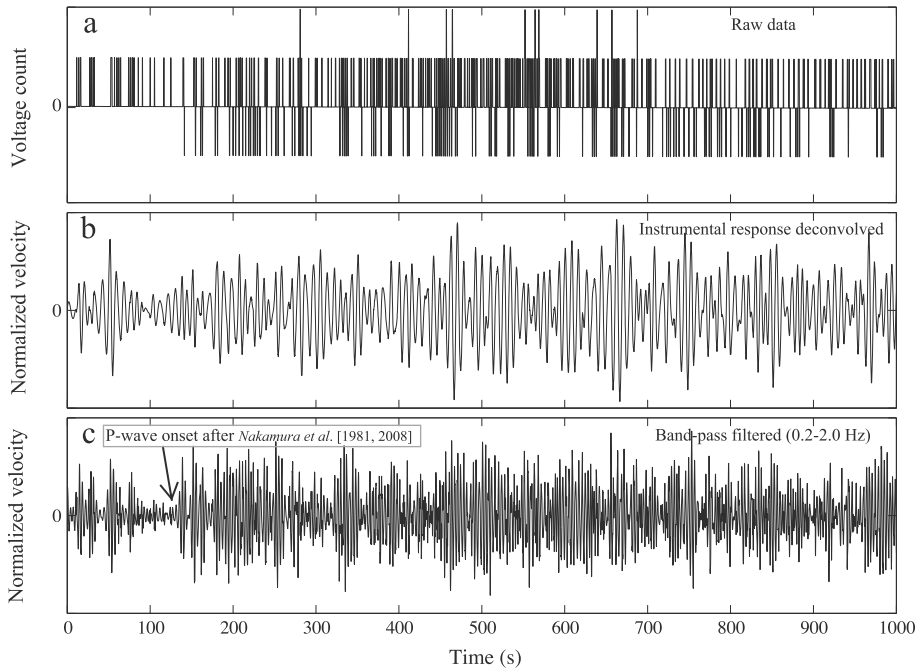

Figure 4. (a) Raw data of a deep moonquake from cluster A40 as recorded by the vertical component of Station 12 with origin time at 16:15 on 15 April 1972 [*Nakamura et al.*, 1981]. The *P* wave onset is expected to be at 120 s. (b) The seismogram after deconvolution of the station's instrument response. (c) The seismogram after applying a band-pass filter (fifth-order Butterworth filter) between 0.2 Hz and 2 Hz.

moonquake from cluster A40. The onset of the *P* wave phase is seen at 120 s [*Nakamura et al.*, 1981]. In Figure 4b we show the seismogram after instrument-response deconvolution, while in Figure 4c we show the seismogram (trace) from Figure 4b after the band-pass filtering. Note that interpreting an event among several stations is generally known to be difficult as different stations have different SNR. This makes exact arrival time picking of the direct *P* wave phase difficult. Because of this, picking arrival times for both *P* and *S* phases is commonly done for each station on the resulting trace from stacking individual traces from a cluster [e.g., *Bulow et al.*, 2005, 2007; *Nakamura*, 2005]. A relevant discussion and a few examples can be found in *Nakamura* [2005] (Figures 1 and 2 in his report). Even if the data are low bit in appearance (e.g., Figure 4a), one can still retrieve desired signals by SI if such signals are repetitive [e.g., *Derode et al.*, 1999; *Montaldo et al.*, 2002; *Larose et al.*, 2004; *Sens-Schönfelder and Larose*, 2010].

After filtering, we perform a manual QC on each event waveform to decide whether to use it further for DMSI. Spiky and/or amplitude-saturated traces are discarded from further processing. Examples for both used and discarded traces are shown in Figure 5. A summary of the number of the event data before and after QC is given in Table 1.

Subsequently, we extract the *P* wave coda from all vertical-component traces that are selected for further processing. The extraction is done using a time window starting 5 s after the onset of the direct *P* wave phase (based on *Nakamura et al.* [1981]) and finishing before the onset of the direct *S* wave phase. Although in DMSI we use only the vertical-component data, as described above, we use also the transverse-component data to aid us in identifying the onset of the direct *S* wave phase since *S* wave phases are generally clearer on the transverse (Figure 5). For the recordings at Apollo stations 12 and 14, we also use the published onset times of the direct *S* wave phases provided by *Nakamura* [1983].

As reported in previous studies, the precise arrival times for the direct *P* wave phases are sometimes difficult to identify [e.g., *Nakamura*, 2005]. Since we use for DMSI the *P* wave coda as input data, however, precise arrival times are not needed. Needless to say, it would be advantageous to be able to identify the precise onset of the direct *P* wave phases so that a longer time window of the *P* wave coda could be used. This could permit retrieval of reflections from, and thus imaging of, deeper structures, via DMSI. Due to the uncertainty of the *P* wave onset, the length of the *P* wave coda tends to be shorter. Because of the onset-time uncertainty,

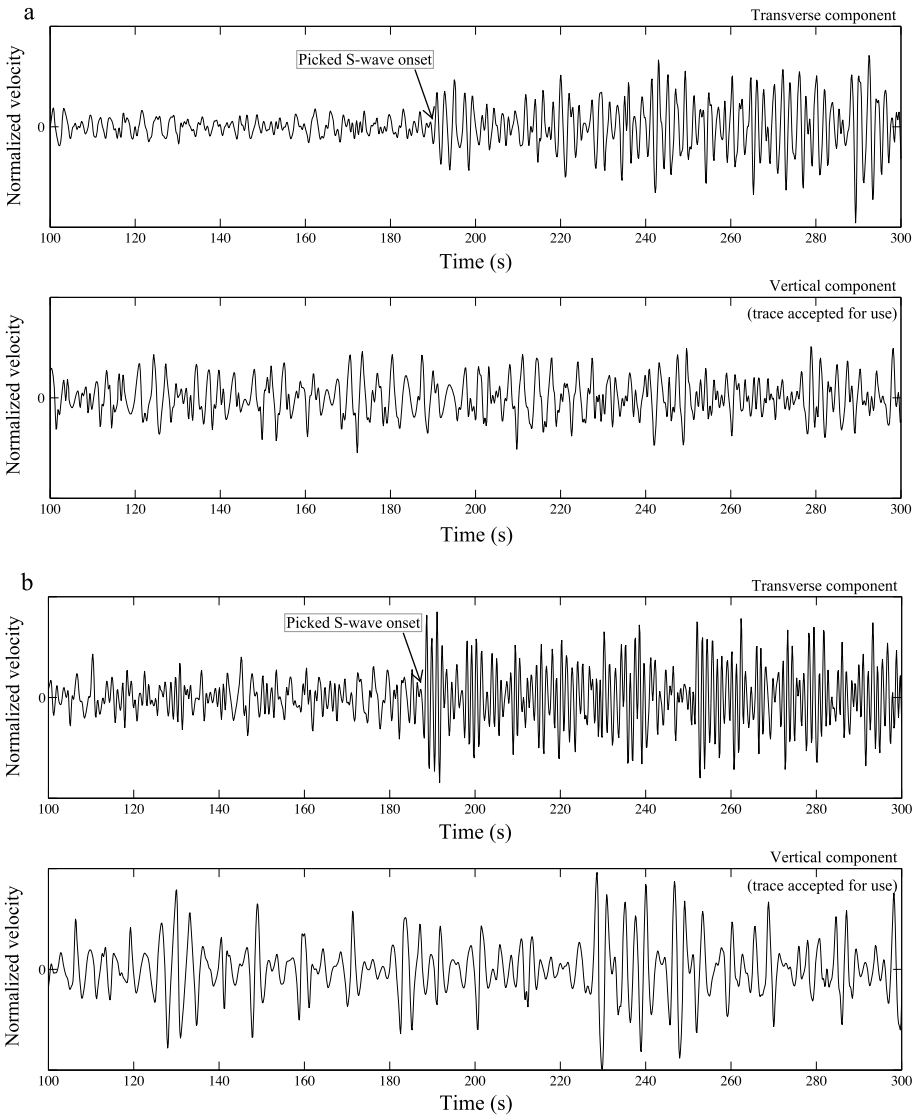

Figure 5. Examples of used and discarded seismograms (traces) after applying the data processing of Figure 4. (a) Traces of a deep moonquake at 06:11 on 19 May 1977 from cluster A97 recorded by Station 16. The vertical-component trace is used for further processing. (b) Traces of a deep moonquake from cluster A9 at 22:32 on 4 December 1971, recorded by Station 14. The vertical-component trace is used for further processing. (c) Spiky traces of a deep moonquake from cluster A15 occurring at 14:31 on 18 February 1972 recorded by Station 14. The vertical-component trace is discarded from further processing. (d) Ringing traces of a deep moonquake from cluster A9 recorded at Station 14 from 04:16 on 29 January 1972. The vertical-component trace is discarded from further processing. The origin times are from *Nakamura et al.* [1981].

our *P* wave coda extraction windows begin 5 s after the estimated onset of the direct *P* wave phase. Note that the maximum two-way travel time we can retrieve (and thus image) via DMSI using the *P* wave coda is less than 50 s (Figure 2). A further advantage is gained by excluding the *P* wave coda after the direct *S* wave arrival, to exclude strong surface wave energy. We assume that the most energetic surface waves begin almost simultaneously with the direct *S* wave arrival. Moreover, the frequency bandwidth we use (0.2–2.0 Hz) reduces surface wave noise, which resides largely in the 4–12 Hz band [*Larose et al.* 2005]. Surface wave contamination may still exist, but much of it will be random; the stacking process used in DMSI will suppress such noise. At the same time, DMSI enhances the repeatable signals (e.g., reflections). We acknowledge the possibility that DMSI may retrieve scattered surface waves from repeatable scattering due to *P* wave conversions arriving ahead of the *S* wave. Given this, and other possible concerns (e.g., multiple reflections), we focus our interpretation only on major subsurface features (if present).

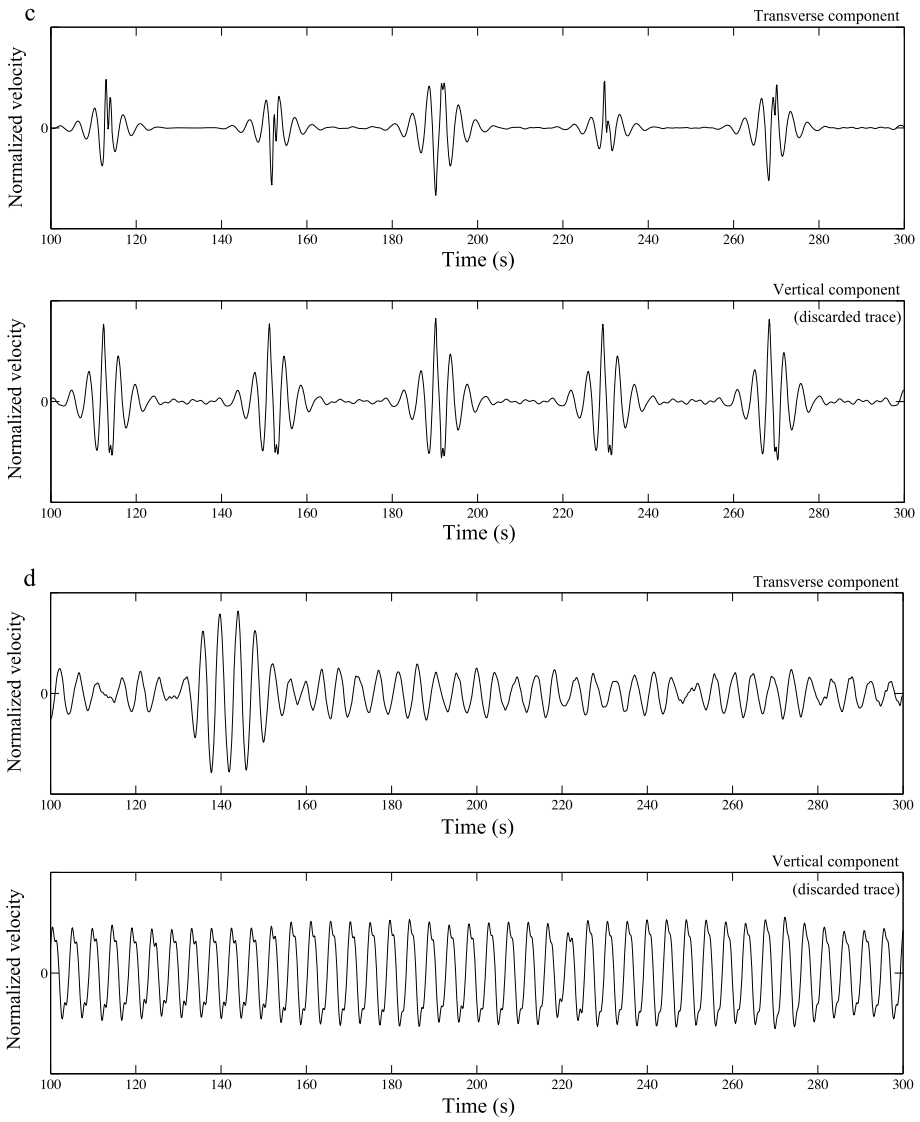

Figure 5. (continued)

After extraction of the *P* wave coda from the selected traces, we apply energy normalization (to their respective maxima) to each selected trace. This normalization effectively removes the magnitude differences among moonquakes within a cluster and equalizes the amplitudes. After normalization we apply DMSI.

To retrieve the zero-offset vertical-incidence plane-wave response, one can take two approaches. Following the first technique, all normalized *P* wave coda traces from deep moonquakes pertaining to one cluster are summed together (stacked). This would result in improved SNR also of later arrivals. DMSI is applied to the resulting stacked trace. If the event locations for one cluster are sufficiently close to one another, the stacked trace will be characterized by an improved SNR of the reverberations, providing clear retrieved reflections. Figures 6a–6g (left column) show the retrieved zero-offset reflection trace resulting from the application of DMSI to the stacked trace. This approach will produce meaningful results only when the moonquake hypocenters in a cluster are very close to one another both laterally and in depth. Hence, this approach serves as a test of hypocentral proximity within a cluster.

In the alternative approach, DMSI is applied by autocorrelating each of the normalized *P* wave coda traces from deep moonquakes within one cluster and stacking them. Figures 6a–6g (middle column) show the autocorrelation results for all selected traces in each cluster we use, while Figures 6a–6g (right column) show the result from stacking the autocorrelated traces from the respective middle column. If the event locations for one cluster are sufficiently close to one another, the retrieved traces in Figures 6a–6g (left and right

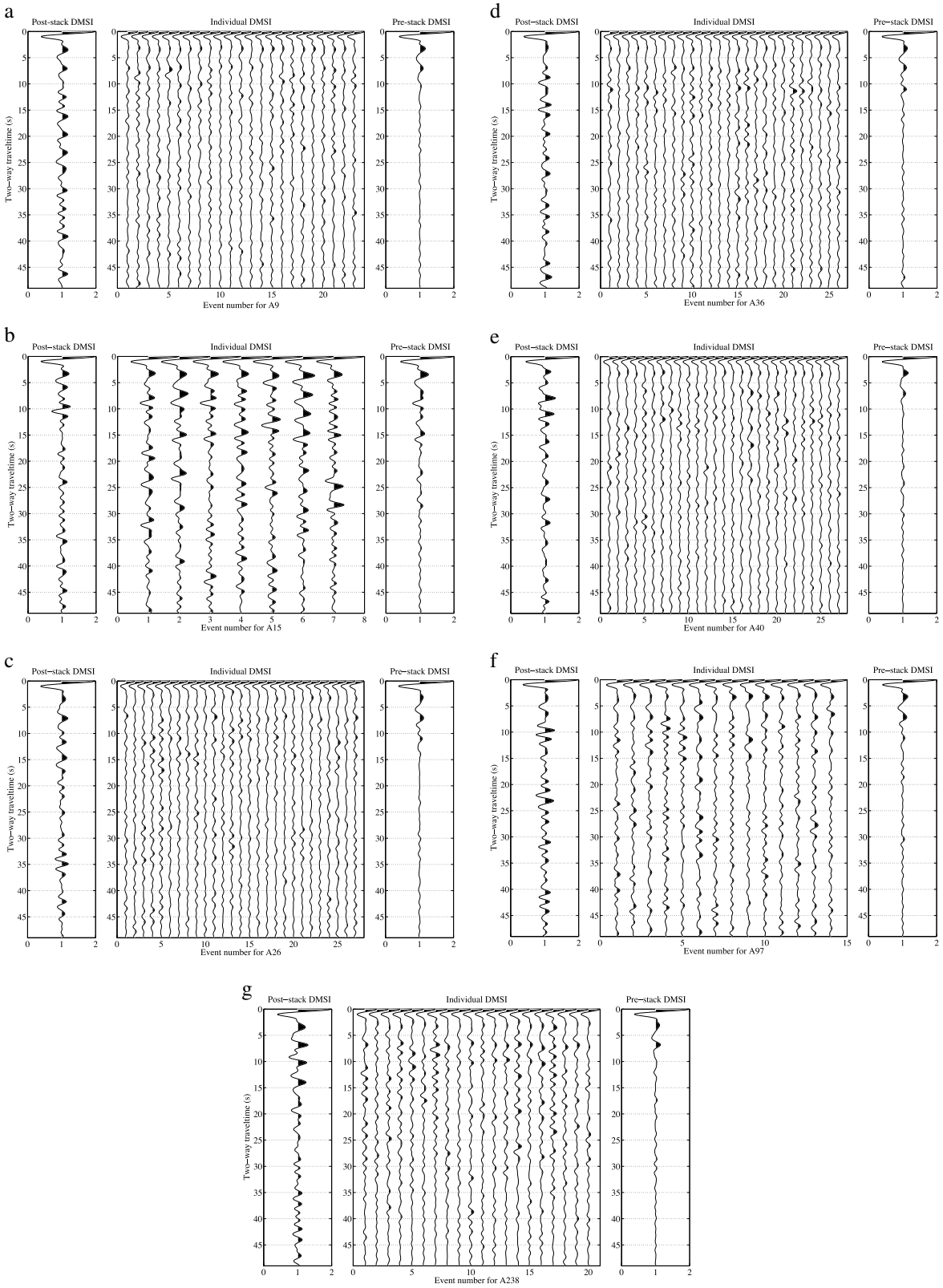

Figure 6. Results in two-way travel time retrieved by DMSI for our selected clusters: (a) A9. (b) A15. (c) A26. (d) A36. (e) A40. (f) A97. (g) A238. Figures 6a–6g (left column) represent DMSI results obtained from autocorrelation of the stacked *P* wave codas for one cluster. Figures 6a–6g (middle column) show the individual autocorrelations for each selected *P* wave coda for one cluster recorded by one station. Figures 6a–6g (right column) show the retrieved DMSI result after stacking the traces in the middle column.

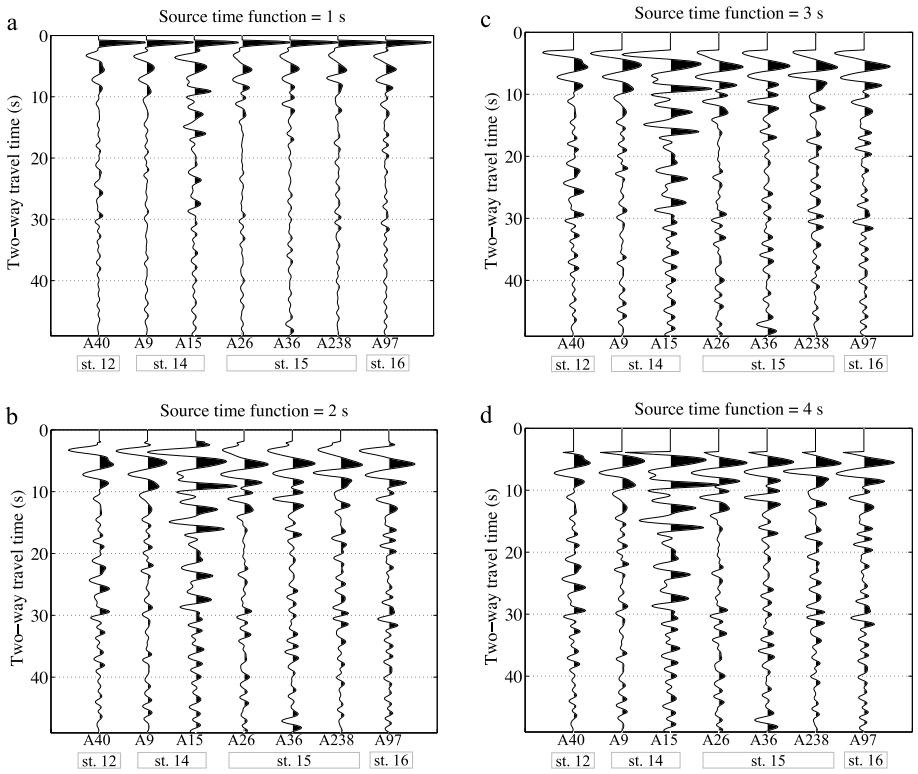

Figure 7. A comparison of the retrieved DMSI result (the right panels in Figure 6) when the averaged source time function $\overline{M}_k(t)$ is muted down to (a) 1 s, (b) 2 s, (c) 3 s, and (d) 4 s.

columns) should exhibit the same retrieved reflections, although the right column may exhibit a lower SNR. Figures 6a–6g (left and right columns), though, show different retrieved results. This means that the event locations for one cluster are not sufficiently near to one another laterally and/or vertically (in depth). The horizontal and depth location uncertainties given in Figure 1 (see also Table 1) were calculated based on the error ranges in the locations in *Nakamura* [1983], which he attributed to errors in the velocity model.

Because of the location scatter within each cluster, DMSI response applied to a stacked trace is expected to provide poorer results than the stacking of DMSI results applied to individual traces. The difference arises because when the sources are not sufficiently close to one another, the coda from each source in a cluster has different arrival times and their stack will decrease the SNR. When stacking autocorrelated traces, the situation is different. Autocorrelating the coda from each source separately accounts for differences in the travel times between a source and the surface, as illustrated in Figure 3, thus leaving only the free-surface reverberation (retrieved reflections) in the result. For a sufficient number of events from a cluster, retrieved reflections interfere constructively in the stacking of the autocorrelated traces, so SNR increases. We therefore follow the second path for our full analysis.

After the above processing, from equation (2) we retrieved $-R(\mathbf{x}_R, \mathbf{x}_R, t)$. We multiply this result by -1 to obtain the reflection response $R(\mathbf{x}_R, \mathbf{x}_R, t)$, which is also characterized by a zero-phase wavelet $\overline{M}_k(t)$. This means that in forthcoming figures after Figure 7 one can interpret peaks as positive events (filled in black) and troughs as negative events. These peaks and troughs may be blurred by multiples and their interference as demonstrated in the following section. The estimated source time function for a M_w 3.0 earthquake is $<=1$ s [*Kanamori and Brodsky*, 2004] and the M_w and M_L scales at and below 3.0 are roughly equivalent [*Hanks and Boore*, 1984]. Since the magnitudes of our events are estimated to be no greater than M_L 1.3 [*Lammiein*, 1977] or 3.0 [*Minshull and Goulty*, 1988], the first 3 s should sufficiently capture the autocorrelated source time functions. We therefore mute the first 3 s in the correlation result to suppress the autocorrelated source time function (i.e., the first term on the right-hand side of equation (2) after convolution). To verify that muting of the first 3 s is sufficient, we compared the suppression using different durations for the autocorrelated source time

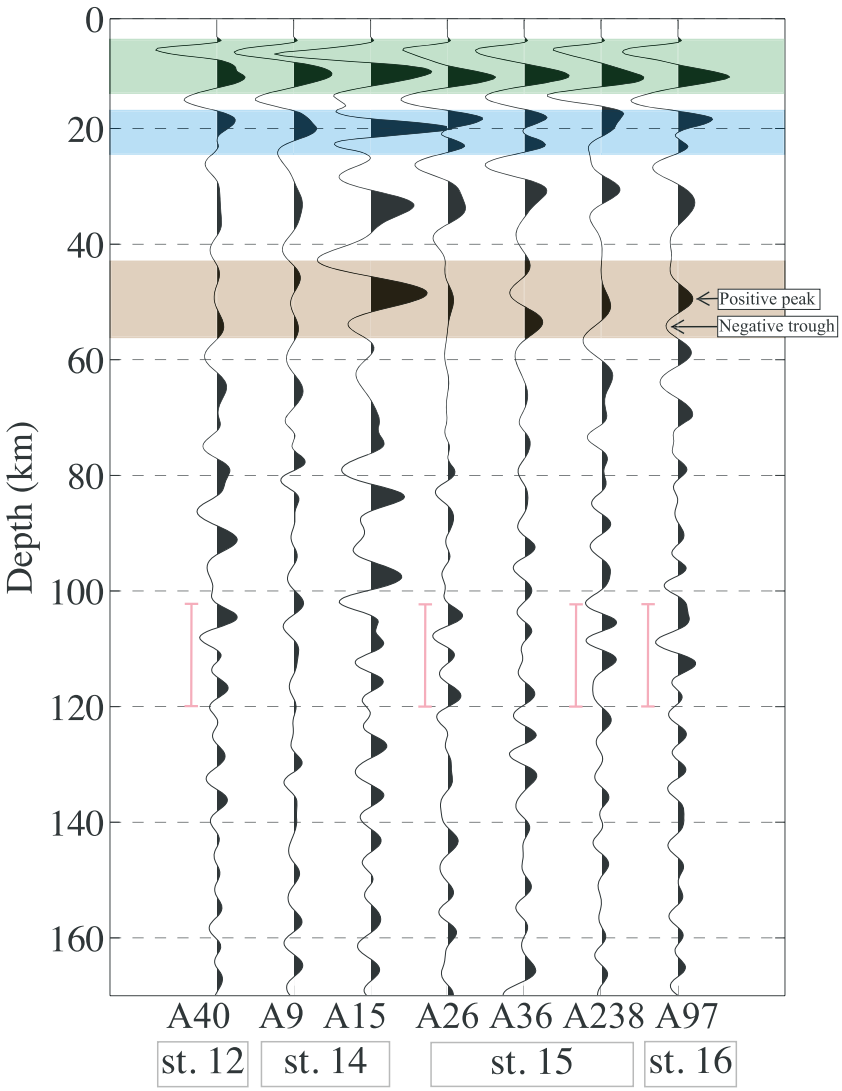

Figure 8. Images in depth, with highlighted horizons, obtained from the DMSI results. The transparent green indicates a possible tuned thin-layer reflection from the megaregolith layer (e.g., a depth of 1 km in *Cooper et al.*, [1974]). The transparent blue rectangle indicates the zone where not only the reflection from the acoustic boundary at ~ 20 km depth but also two different ghosts: one is the interfered response between the responses from the boundary at ~ 1 km and ~ 20 km; and the other is at ~ 20 km and the Moho would contribute. The pink bars indicate parts of the upper mantle characterized by laterally coherent horizons under some of the stations. The transparent brown rectangle indicates the zone where we interpret the Moho. Two black arrows indicate the definition of our positive peak and negative trough, respectively.

functions, ranging from 1 s to 4 s with time step of 1 s. The results of the suppressions are shown in Figures 7a–7d. Any of the three results from 2 s to 4 s can be also used; however, we choose 3 s, as we find this result clearer for interpretation of the shallower part of the retrieved reflection response. If needed, one can also try to remove the source time functions for arrivals later than 3 s. Results would be only improved, however, when individual source time functions are well estimated. In this study, since the magnitude of the deep moonquakes is expected to be rather small [e.g., *Lammiein*, 1977], the retrieved source time function will not be long and thus will not hamper our interpretations of the dominant features (e.g., the Moho).

As a final step, the DMSI results are converted from two-way travel time to depth (Figure 8) using the Dix's equation [*Yilmaz*, 1987] making use of the 1-D velocity model of *Weber et al.* [2011]. We include in the model the local thickness (1 km) of the megaregolith whose velocity is estimated to be 1 km/s. Without the low-velocity megaregolith, the estimated depth of the Moho would be few kilometers deeper than the 50 km of Figure 8.

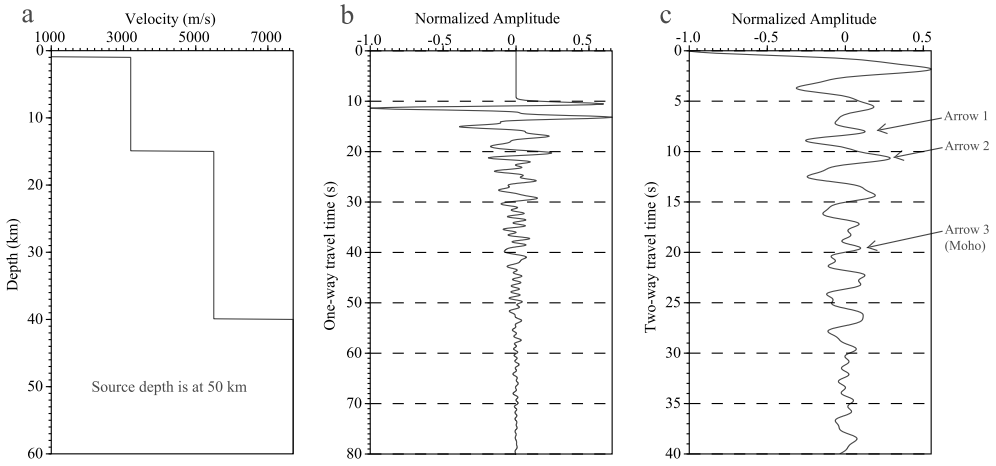

Figure 9. (a) The 1-D velocity model of *Weber et al*. [2011]. (b) The transmission response from the source radiated from a depth of 50 km and recorded at the surface. (c) The retrieved reflection response obtained by DMSI (autocorrelation) of the coda of the response in Figure 9b with three examples of events indicated by Arrow 1 where an expected arrival time for the ghost caused by interfering responses from a depth of 1 km and 15 km appears at 8.7 s as well as the one from a depth of 15 km and 40 km arrives at 9.1 s; Arrow 2 where an expected arrival time for the reflection from a depth of 15 km appears at 10.7 s; and Arrow 3 where an expected arrival time for the reflection from a depth of 40 km (the modeling Moho) appears at 19.8 s.

5. Numerical Wavefield Modeling

In order to aid the interpretation of the DMSI results (Figure 8), we perform 1-D numerical modeling for DMSI using a 2-D finite-difference modeling code in acoustic mode [*Thorbecke and Draganov*, 2011]. The 1-D model we used (Figure 9a) is taken from *Weber et al*. [2011]. We use it to model transmission responses from subsurface sources at a depth of 50 km clustered laterally within 2 km around the lateral position of the station, with 200 m source spacing. The retrieved reflection at the surface (Figure 9c) is obtained by autocorrelating the transmission responses from each source (e.g., in Figure 9b for the source vertically below the station) and summing the separate autocorrelations. We use a Ricker wavelet [*Yilmaz*, 1987] with a center frequency of 0.5 Hz to approximate the DMSI result for cluster A97. Note that the impedance boundary at a depth of 40 km is the Moho in this model. Having sources at a depth of 50 km and laterally close to the station ensures nearly vertical illumination of the station. As in the previous section, the direct *P* wave arrival in the transmission from each source has been muted. The total modeling length of 80 s simulates an average length of the recordings used in the previous section between the direct *P* wave and *S* wave phases.

For the model in Figure 9a, the expected retrieved zero-offset reflections from the three impedance contrasts at 1 km, 15 km, and 40 km should appear at 2 s, 10.75 s (Arrow 2 in Figure 9c), and 19.85 s (Arrow 3 in Figure 9c). The reflection from the Moho marks a major characteristic difference between earlier and later package of responses. The earlier responses (0–17 s) show relatively higher amplitudes and broad phases, whereas later responses ($>$22 s) are characterized by relatively lower amplitudes and ringing phases. We note other arrivals as well. For example, an event is seen with a positive peak at 8 s (Arrow 1 in Figure 9c) and a negative peak at 9.1 s. This is an artifact caused by the interference of multiple reflections (multiples) within the shallowest layer of 1 km thickness and the reflection from the impedance contrast at 15 km. Other arrivals not discussed here are combinations between multiples and between multiples and primary reflections. Note that the primary reflection from the low-velocity layer at 1 km cannot be retrieved as a separate reflection but forms part of the virtual-source time function (tuning effect).

We see based on the modeling results that if low-velocity layers are indeed present beneath our Apollo stations, it would introduce difficulties in distinguishing within the DMSI field results which events arise from which layers. Nevertheless, we are able to identify the Moho via the major characteristic change of waveform for earlier versus later arrivals. If the DMSI results illuminate features similar to those from our numerical modeling, such features are consistent with the impedance boundaries within our velocity model.

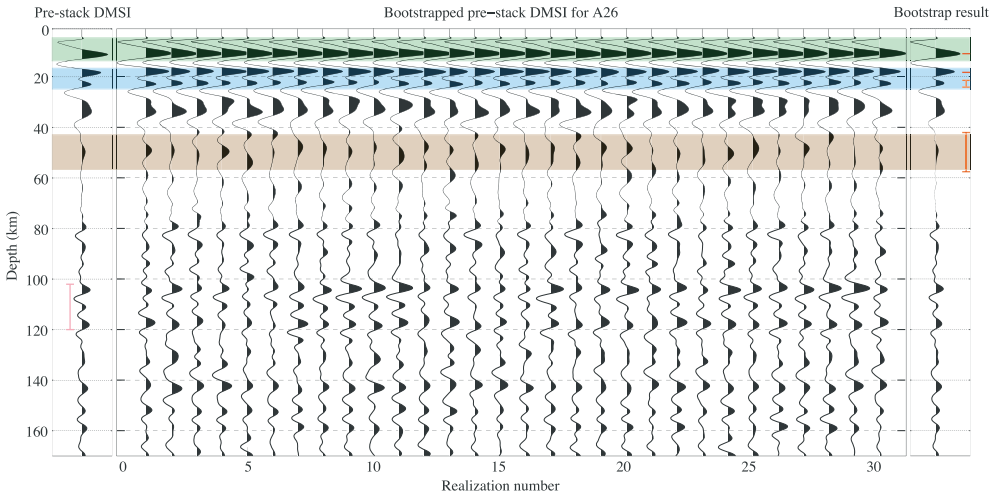

Figure 10. The result of a bootstrap test for the A26 cluster. Transparent rectangles follow the interpretation from Figure 8. Orange bars in the right panel indicate 95% confidence interval for the positive peaks in the transparent rectangles.

6. Results and Discussion

Figure 8 shows the DMSI traces for our selected clusters, presented on a depth axis rather than time axis. We interpret consistent peaks and troughs as delineating reflectors below the Apollo stations from each of the seven clusters that we used. One of the most striking features is that for all clusters the strongest amplitudes appear laterally coherent at depths of around 5 km and 13 km as a trough and a peak, respectively (the transparent green rectangle in Figure 8). Based on the numerical modeling, this may represent a tuned thin-layer reflection from the megaregolith layer (e.g., a depth of 1 km in *Cooper et al.* [1974]). By "tuned thin-layer reflection," we mean that the observed waveform arises from interference between two or more reflections at impedance boundaries which are less than one quarter wavelength from one another in depth. The only exception is cluster A15, whose direct *P* wave arrivals exhibit the highest ray parameter among the clusters used (see Table 1). This cluster is the smallest following QC, hence, we may simply not be benefiting from stacking to the extent that larger clusters provide. The package of relatively strong and laterally coherent amplitudes continues to a depth of 42 km. Below this depth, we see relatively lower amplitudes with ringing phases. This characteristic, which is manifested both shallower and deeper than about 50 km, may be viewed as an analogue to the zero-offset trace obtained through synthetic modeling in Figure 9c. The Moon's Moho in that case delineated a boundary between the two distinct zones. We therefore interpret the field results as marking the Moho at about 50 km depth. It is difficult to determine the exact Moho depth, however, because the Moho reflection may be affected by interference from multiples, which depend on the number and depth of unmodeled layers. Uncertainty in our interpretation of the Moho depth is captured by the transparent brown rectangle in Figure 8. This rectangle highlights the feature related to the retrieved Moho reflection indicated by Arrow 3 in Figure 9c. Thus, we estimate the depth of the Moho as 50 ± 8 km beneath the Apollo stations when relying upon the velocity model in *Weber et al.* [2011] for our analysis. The lower boundary of the region containing the Moho (the transparent brown rectangle in Figure 8) we set at 58 km because of stronger-amplitude events beneath it (e.g., positive peaks around 60–65 km at A9, A40, and A238). Such events are also present in the synthetic results. Using the events indicated by Arrow 1 and Arrow 2 in Figure 9c, the strong positive amplitudes around 20 km in Figure 8 (highlighted by the transparent blue rectangle) can be interpreted as a reflection from an impedance contrast at that depth, although we cannot rule out artifacts. The laterally coherent event at around 30–35 km depth may arise from either an impedance boundary or a multiple of the event in the transparent green rectangle in Figure 8. In other words, our method supports the presence of layers shallower than the Moho [e.g., *Cooper et al.*, 1974], but due to the few available stations this cannot be determined unequivocally.

To validate our discussed interpretation for Figure 8, we performed a bootstrap test on the cluster A26, which contains the largest number of deep moonquakes (Figure 10). In this test, we randomly select 20 of the 27 DMSI traces to produce a stack and repeat this procedure 30 times. Our interpretation (transparent rectangles) in Figure 8 is superimposed on the bootstrap results in Figure 10. Figure 10 (right) is the

mean of the individual bootstrapping realizations (Figure 10, middle). After picking the maximum positive amplitude from the individual bootstrapping realizations for the transparent rectangles, we calculate the 95% confidence intervals, shown as orange bars in Figure 10 (right). It turns out that our interpretation for the transparent rectangles in green and blue has an uncertainty in depth of less than 1 km. For the Moho interpretation (the transparent rectangle in brown), the uncertainty is about ± 8.5 km from the mean depth of 50 km, supporting our qualitative Moho interpretation of 50 km ± 8 km.

Looking at regions below the Moho, the image suggests, in general, a laterally heterogeneous subsurface. This agrees with our synthetic model, which indicates that such a lateral feature arises when no significant velocity layers exist. We do, however, note some coherent features under two or three of the stations and at different depths: a well-correlated trough for stations 12, 15, and 16 at 100–120 km (indicated by the pink bars) for clusters A40, A26, A238, and A97.

A variety of studies using various methods have suggested different depths to the Moho on the Moon, thus lunar crustal thickness is still unresolved, as well as how much this thickness may vary spatially. Estimates of crustal thickness ranging from 30 to 60 km, arrived at through various analytical methods, are in rough agreement with our 42–58 km estimate, but the wide range of values may be consequential to models for the evolution of the Moon; hence, the accurate determination of lunar crustal thickness is pivotal to developing lunar genesis models.

Our DMSI result (Figure 8) provides the first reflection imaging using natural moonquakes. We find relatively higher-amplitude arrivals characterized by lateral coherency at depths of ~ 50 km. This zone is generally characterized by a weak triple peaks/trough feature and is about 10 km thick (the transparent brown rectangle in Figure 8). We interpret this characteristic feature at 50 km depth as the reflection from the lunar Moho beneath our stations with an uncertainty of ± 8 km. This agrees with the interpretation from *Khan et al*. [2000] and *Ishihara et al*. [2009] and is close to the results reported by *Nakamura* [1983] and from the deepest level of the Moho as interpreted from the GRAIL data. Our results may be useful to constrain velocity modeling such as *Wieczorek et al*. [2013] at the four Apollo stations.

Below 58 km, waveforms exhibit generally incoherent features, suggesting laterally heterogeneous structure. In previous studies, *Dainty et al*. [1974], *Nakamura et al*. [1976], and *Goins et al*. [1981] suggested that the seismic attenuation in the upper mantle is very low ($Q = 3000–5000$). This is consistent with the very long codas exhibited by moonquakes. The weak suggestion of a consistent horizontal feature in Figure 8 at a depth of roughly 100–120 km (the pink bars) combined with the lack of pronounced lateral coherency in the deeper part of our image suggests the presence of a strong scattering zone, consistent with previous studies that yield no clear velocity structure around this depth range [e.g., *Toksöz*, 1974; *Goins et al*., 1981] and the roughly uniform velocity at depth proposed by *Weber et al*. [2011].

The average estimated hypocentral depth for the 28 shallow moonquakes is ~ 95 km, (derived from *Nakamura et al*. [1981]). Depths of the shallow moonquakes near the Apollo stations vary from about 100 km to 129 km that is within the heterogeneous zone observed in our analysis. The lack of observed structure in the source region might point to the assertions that these events do not arise from any lunar tectonic process, but rather may be the result of tidal stresses [e.g., *Toksöz et al*., 1977; *Frohlich and Nakamura*, 2009; *Weber et al*., 2009]. If more stations and/or arrays are deployed, however, one might be able to interpret structures at these depths in the region of the Apollo stations. We therefore cannot exclude the possibility that these events are tectonic in nature [*Oberst*, 1987].

DMSI may also be applied for imaging structures under future seismic deployments on the farside of the Moon if stations are optimally located with respect to seismicity. It might be feasible to use deep moonquakes from the nearside, assuming adequate SNR after phase propagation to the farside. Ray parameters in this case should be sufficiently small at the farside stations to allow application of the traditional SI using directly transmitted *P* wave phases and their reverberations (equation 1). DMSI using the nearside deep moonquakes may likewise be feasible.

7. Conclusions

We have applied seismic interferometry to *P* wave codas of deep moonquakes (DMSI) recorded by the Apollo seismic stations to retrieve a reflection image of the Moon's subsurface. With DMSI, we analyzed the *P* wave

coda of seven clusters of deep moonquakes whose incoming wavefronts of the direct *P* wave phases are approximately planar at the stations, and whose ray parameters are sufficiently small. Our DMSI image shows reflections consistent with structures at depths of ~5 km to ~170 km beneath the Apollo stations on the nearside of the Moon. The image reveals laterally coherent horizontal events with strong amplitudes under all four Apollo stations down to a depth of 50 km, where we observe a laterally coherent horizon characterized by relatively lower amplitudes. Below that horizon, our results are characterized by rather ringing phases with relatively lower amplitude. We interpret the acoustic boundary at 50 km to be the lunar Moho beneath the four Apollo stations with an uncertainty of ±8 km due to possible interference from multiple reflections. This depth value is in good agreement with JAXA's SELENE study and is close to the depth in previous travel time studies. The deeper part of the image reveals a laterally heterogeneous picture with very few laterally coherent horizontal events interpretable beneath three of the Apollo stations. These suggest the presence of a strong scattering zone. Our results show that DMSI has the potential to obtain zero-offset reflection images without the need of active sources, such as explosives or other artificial impacts. Our method could be extended to imaging the subsurface below seismic stations on the farside of the Moon if installed by future missions.

Acknowledgments

The data used in this study were collected using the Moon Seismic Monitor (http://darts.isas.jaxa.jp/planet/seismology/apollo/app/) of the Data Archives and Transmission System (DATS, darts.jaxa.jp), provided by the Center for Science-satellite Operation and Data Archive (C-SODA, http://c-soda.isas.jaxa.jp) at the Institute of Space and Astronautical Science (ISAS, http://www.isas.jaxa.jp/e/index.shtml) and the Japan Aerospace Exploration Agency (JAXA, http://global.jaxa.jp). The facilities of IRIS Data Services, and specifically the IRIS Data Management Center, were used for access to waveforms, related metadata, and/or derived products used in this study. IRIS Data Services are funded through the Seismological Facilities for the Advancement of Geoscience and EarthScope (SAGE) Proposal of the National Science Foundation under Cooperative Agreement EAR-1261681. This research is supported by the Division for Earth and Life Sciences (ALW) with financial aid from the Netherlands Organization for Scientific Research (NWO) with grant VIDI 864.11.009. This is Los Alamos National Laboratory Publication LA-UR-15-27729. The maps were drawn with Generic Mapping Tool (GMT) [*Wessel and Smith*, 1991]. The travel times for the Moon were calculated using the TauP Toolkit [*Crotwell et al.*, 1999]. We are grateful to S.A. Hauck II, Editor in Chief, and two anonymous reviewers for their very constructive comments that helped improve the quality of the manuscript.

References

Aki, K. (1957), Space and time spectra of stationary waves with special reference to microtremors, *Bull. Earthquake Res. Inst. Univ. Tokyo*, *35*, 415–456.

Araki, H., et al. (2009), Lunar global shape and polar topography derived from Kagura-LALT laser altimetry, *Science*, *323*, 897–900, doi:10.1126/science.1164146.

Besserer, J., F. Nimmo, M. A. Wieczorek, R. C. Weber, W. S. Kiefer, P. J. McGovern, J. C. Andrews-Hanna, D. E. Smith, and M. T. Zuber (2014), GRAIL gravity constraints on the vertical and lateral density structure of the lunar crust, *Geophys. Res. Lett.*, *41*, 5771–5777, doi:10.1002/2014GL060240.

Blanchette-Guertin, J.-F., C. L. Johnson, and J. F. Lawrence (2012), Investigation of scattering in lunar seismic coda, *J. Geophys. Res.*, *117*, E06003, doi:10.1029/2011JE004042.

Bulow, R. C., C. L. Johnson, and P. M. Shearer (2005), New events discovered in the Apollo lunar seismic data, *J. Geophys. Res.*, *110*, E10003, doi:10.1029/2005JE002414.

Bulow, R. C., C. L. Johnson, B. G. Bills, and P. M. Shearer (2007), Temporal and spatial properties of some deep moonquake clusters, *J. Geophys. Res.*, *112*, E09003, doi:10.1029/2006JE002847.

Chapman, W. B., B. M. Middlehurst, and A. L. Frisillo (1974), Moonquake predetermination and tides, *Icarus*, *21*, 427–436, doi:10.1016/0019-1035(74)90145-6.

Chenet, H., P. Longnonné, M. Wieczorek, and H. Mizutani (2006), Lateral variations of lunar crustal thickness from the Apollo seismic data set, *Earth Planet. Sci. Lett.*, *243*, 1–14, doi:10.1016/j.epsl.2005.12.017.

Claerbout, J. (1968), Synthesis of a layered medium from its acoustic transmission response, *Geophysics*, *33*, 264–269, doi:10.1190/1.1439927.

Cooper, M., R. L. Kovach, and J. S. Watkins (1974), Lunar near-surface structure, *Rev. Geophys.*, *12*, 291–308, doi:10.1029/RG012i003p00291.

Crotwell, H. P., T. J. Owens, and J. Ritsema (1999), The TauP Toolkit: Flexible seismic travel-time and ray-path utilities, *Seismol. Res. Lett.*, *70*, 154–160, doi:10.1785/gssrl.70.2.154.

Dainty, A. M., M. N. Toksöz, K. R. Anderson, and P. J. Pines (1974), Seismic scattering and shallow structure of the Moon in oceanus procellarum, *Moon*, *9*, 11–29, doi:10.1007/BF00565388.

Derode, A., A. Tourin, and M. Fink (1999), Ultrasonic pulse compression with one-bit time reversal through multiple scattering, *J. Appl. Phys.*, *85*, 6343, doi:10.1063/1.370136.

Draganov, D., R. Ghose, E. Ruigrok, and J. Thorbecke (2010), Seismic interferometry, intrinsic losses and Q-estimation, *Geophys. Prospect.*, *58*, 361–373, doi:10.1111/j.1365-2478.2009.00828.x.

Frohlich, C., and Y. Nakamura (2009), The physical mechanisms of deep moonquakes and intermediate-depth earthquakes: How similar and how different? *Phys. Earth Planet. Inter.*, *173*, 365–374, doi:10.1016/j.pepi.2009.02.004.

Goins, N. R. (1978), Lunar seismology: The internal structure of the moon, PhD thesis, 666 pp., Mass. Inst. of Technol., Cambridge, Mass.

Goins, N. R., A. A. Dainty, and M. N. Toksöz (1981), Lunar seismology: The internal structure of the Moon, *J. Geophys. Res.*, *86*, 5061–5074, doi:10.1029/JB086iB06p05061.

Hanks, T. C., and D. M. Boore (1984), Moment-magnitude relations in theory and practice, *J. Geophys. Res.*, *89*, 6229–6235, doi:10.1029/JB089iB07p06229.

Horvath, P., G. V. Latham, Y. Nakamura, and H. J. Dorman (1980), Lunar near-surface shear wave velocities at the Apollo landing sites as inferred from spectral amplitude ratios, *J. Geophys. Res.*, *85*, 6572–6578, doi:10.1029/JB085iB11p06572.

Ishihara, Y., T. Morota, R. Nakamura, S. Goossens, and S. Sasaki (2009), Crustal thickness of the Moon: Implications for farside basin structures, *Geophys. Res. Lett.*, *36*, L19202, doi:10.1029/2009GL039708.

Kanamori, H., and E. E. Brodsky (2004), The physics of earthquakes, *Rep. Prog. Phys.*, *67*, 1429–1496, doi:10.1088/0034-4885/67/8/R03.

Khan, A., K. Mosegaard, and K. L. Rasmussen (2000), A new seismic velocity model for the Moon from a Monte Carlo inversion of the Apollo lunar seismic data, *Geophys. Res. Lett.*, *27*, 1591–1594, doi:10.1029/1999GL008452.

Khan, A., A. Pommier, G. A. Neumann, and K. Mosegaard (2013), The lunar Moho and the internal structure of the Moon: A geophysical perspective, *Tectonophysics*, *609*, 331–352, doi:10.1016/j.tecto.2013.02.024.

Kimman, W. P., and J. Trampert (2010), Approximations in seismic interferometry and their effects on surface waves, *Geophys. J. Int.*, *182*, 461–476, doi:10.1111/j.1365-246X.2010.04632.x.

Lammiein, D. R. (1977), Lunar seismicity and tectonics, *Phys. Earth Planet. Inter.*, *14*, 224–273, doi:10.1016/0031-9201(77)90175-3.

Larose, E., A. Derode, M. Campillo, and M. Fink (2004), Imaging from one-bit correlations of wideband diffuse wave fields, *J. Appl. Phys.*, *95*, 8393, doi:10.1063/1.1739529.

Larose, E., A. Khan, Y. Nakamura, and M. Campillo (2005), Lunar subsurface investigated from correlation of seismic noise, *Geophys. Res. Lett.*, *32*, L16201, doi:10.1029/2005GL023518.

Latham, G., M. Ewing, F. Press, and G. Sutton (1969), The Apollo passive seismic experiment, *Science*, *169*, 241–250, doi:10.1126/science.165.3890.241.

Longnonné, P., J. Gagnepain-Beyneix, and H. Chenet (2003), A new seismic model of the Moon: Implications for structure, thermal evolution and formation of the Moon, *Earth Planet. Sci. Lett.*, *211*, 27–44, doi:10.1016/S0012-821X(03)00172-9.
Minshull, T. A., and N. R. Goulty (1988), The influence of tidal stresses on deep moonquake activity, *Phys. Earth Planet. Inter.*, *52*, 41–55, doi:10.1016/0031-9201(88)90056-8.
Montaldo, G., P. Roux, A. Derode, C. Negreira, and M. Fink (2002), Ultrasound shock wave generator with one-bit time reversal in a dispersive medium, application to lithotripsy, *Appl. Phys. Lett.*, *80*, 897, doi:10.1063/1.1446996.
Nakamura, Y. (1983), Seismic velocity structure of the lunar mantle, *J. Geophys. Res.*, *88*, 677–686, doi:10.1029/JB088iB01p00677.
Nakamura, Y. (2005), Farside deep moonquakes and deep interior of the Moon, *J. Geophys. Res.*, *110*, E01001, doi:10.1029/2004JE002332.
Nakamura, Y., F. K. Duennebier, G. V. Latham, and H. J. Dorman (1976), Structure of the lunar mantle, *J. Geophys. Res.*, *26*, 4818–4824, doi:10.1029/JB081i026p04818.
Nakamura, Y., G. V. Latham, H. J. Dorman, and J. E. Harris (1981), Passive seismic experiment long-period event catalog. Final version, *Tech. Rep. 18*, Inst. Og Geophys., Univ. of Tex., Galveston. [Revised, (2008)].
Nakamura, Y., G. V. Latham, and H. J. Dorman (1982), Apollo lunar seismic experiment—Final summary, *J. Geophys. Res.*, *87*, A117–A123, doi:10.1029/JB087iS01p0A117.
Obermann, A., T. Planès, E. Larose, and C. Sens-Schönfelder (2013), Depth sensitivity of seismic coda waves to velocity perturbations in an elastic heterogeneous medium, *Geophys. J. Int.*, *194*, 372–382, doi:10.1093/gji/ggt043.
Oberst, J. (1987), Unusually high stress drops associated with shallow moonquakes, *J. Geophys. Res.*, *92*, 1397–1405, doi:10.1029/JB092iB02p01397.
Ruigrok, E., and K. Wapenaar (2012), Global-phase seismic interferometry unveils P-wave reflectivity below the Himalayas and Tibet, *Geophys. Res. Lett.*, *39*, L11303, doi:10.1029/2012GL051672.
Schuster, G. T. (2009), *Seismic Interferometry*, Cambridge Univ. Press, England.
Schuster, G. T., J. Yu, and J. Rickett (2004), Interferometric/daylight seismic imaging, *Geophys. J. Int.*, *157*, 838–852, doi:10.1111/j.1365-246X.2004.02251.x.
Sens-Schönfelder, C., and E. Larose (2010), Lunar noise correlation, imaging and monitoring, *Earthq. Sci.*, *23*, 519–530, doi:10.1007/s11589-010-0750-6.
Snieder, R. (2004), Extracting the Green's function from the correlation of coda waves: A derivation based on stationary phase, *Phys. Rev. E*, *69*, 046610, doi:10.1103/PhysRevE.69.046610.
Tanimoto, T., M. Eitzel, and T. Yano (2008), The noise cross-correlation approach for Apollo 17 LSPE data: Diurnal change in seismic parameters in shallow lunar crust, *J. Geophys. Res.*, *113*, E08011, doi:10.1029/2007JE003016.
Thorbecke, J. W., and D. Draganov (2011), Finite-difference modeling experiments for seismic interferometry, *Geophysics*, *76*, H1–H18, doi:10.1190/GEO2010-0039.1.
Toksöz, M. N. (1974), Geophysical data and the interior of the Moon, *Annu. Rev. Earth Planet. Sci.*, *2*, 151–177, doi:10.1146/annurev.ea.02.050174.001055.
Toksöz, M. N., et al. (1972), Lunar crust: Structure and composition, *Science*, *176*, 1012–1016, doi:10.1126/science.176.4038.1012.
Toksöz, M. N., A. M. Dainty, S. C. Solomon, and K. R. Anderson (1974), Structure of the Moon, *Rev. Geophys.*, *176*, 539–567, doi:10.1029/RG012i004p00539.
Toksöz, M. N., N. R. Goins, and C. H. Cheng (1977), Moonquakes: Mechanisms and relation to tidal stresses, *Science*, *196*, 979–981, doi:10.1126/science.196.4293.979.
Vinnik, L. (2001), First seismic receiver functions on the Moon, *Geophys. Res. Lett.*, *28*, 3031–3034, doi:10.1029/2001GL012859.
Wapenaar, K. (2003), Synthesis of an inhomogeneous medium from its acoustic transmission response, *Geophysics*, *68*, 1756–1759, doi:10.1190/1.1620649.
Wapenaar, K. (2004), Retrieving the elastodynamic Green's function of an arbitrary inhomogeneous medium by cross correlation, *Phys. Rev. Lett.*, *93*, 254301, doi:10.1103/PhysRevLett.93.254301.
Wapenaar, K., J. van der Neut, and E. Ruigrok (2008), Passive seismic interferometry by multidimensional deconvolution, *Geophysics*, *73*, A51–A56, doi:10.1190/1.2976118.
Weber, R. C., B. G. Bills, and C. L. Johnson (2009), Constraints on deep moonquake focal mechanisms through analyses of tidal stress, *J. Geophys. Res.*, *14*, E05001, doi:10.1029/2008JE003286.
Weber, R. C., P. Lin, E. J. Garnero, Q. Williams, and P. Longnonné (2011), Seismic detection of the lunar core, *Science*, *331*, 309–312, doi:10.1126/science.1199375.
Wessel, P., and W. H. F. Smith (1991), Free software helps map and display data, *Eos Trans. AGU*, *72*, 441–448, doi:10.1029/90EO00319.
Wieczorek, M. A., et al. (2013), The crust of the Moon as seen by GRAIL, *Science*, *339*, 671–675, doi:10.1126/science.1231530.
Yilmaz, Ö. (1987), *Seismic Data Analysis*, Society of Exploration Geophysicists, Okla.
Yokoi, T., and S. Margaryan (2008), Consistency of the spatial autocorrelation method with seismic interferometry and its consequence, *Geophys. Prospect.*, *56*, 435–451, doi:10.1111/j.1365-2478.2008.00709.x.
Zhao, D., L. Lei, and L. Liu (2008), Seismic tomography of the Moon, *Chin. Sci. Bull.*, *53*, 3897–3907, doi:10.1007/s11434-008-0484-1.